

# Meshfree modeling the cyclic behavior of sands with large strain Generalized Plasticity

Pedro Navas<sup>a1</sup>, Diego Manzanal<sup>a</sup>, Miguel Martín-Stickle<sup>a</sup>, and Manuel Pastor<sup>a</sup>

<sup>a</sup> *ETSI Caminos, Canales y Puertos, Universidad Politécnica de Madrid.  
c. Prof. Aranguren 3, 28040 Madrid, Spain*

---

## Abstract

Several tools are appreciated when the behavior of permeable sands are to be modeled. First of all, since the movement of the water through the solid skeleton is not negligible, the hypotheses made in the  $u - p_w$  formulation are not considered, since the acceleration of the fluid take an important place in the studied problem. Thus, the complete formulation plays a significant role in a dynamic problem, taking into account that the employment of an appropriate time integration scheme is essential. On the other hand, when considerable movements of the soil are represented, the combination of large deformation schemes within a meshfree framework is known to provide excellent results. In this way, the implementation of the Generalized Plasticity, suitable for modeling sands under dynamic loads, is presented in this work in a finite deformation framework for the first time.

*Keywords:* Generalized Plasticity,  $u - w$  formulation, Optimal Transportation Meshfree, Soil Dynamics, Cyclic

---

## 1. Introduction

The Generalized Plasticity model [1] has been employed successfully in the modeling of sands along the years. Moreover, when cyclic loads appear, this constitutive model is capable to provide useful tools in order to capture  
5 the tension-compression states. Several contributions were made in order to improve the original model in different ways: from the implicit integration of the plastic state [2] to the inclusion of the softening-hardening of the sands with the employment of the state parameter in saturated [3] and unsaturated [4] ....

---

<sup>1</sup>Corresponding author: pedro.navas@upm.es

10 MAS SOBRE PZ  
 MAS SOBRE SANDS-CYCLIC-DRAINED-UNDRAINED

On the other hand, since sands are to be modeled, the intuition make us think that, as the permeability tends to be high, the relative movement of the water phase with respect to the solid one would not be negligible when  
 15 a dynamic problem, such as a high frequency loading, takes place. Thus, the employment of the traditional  $u - p_w$  formulation of the governing equations, even in the dynamic form, is not sufficient to capture the correct acceleration of the water. Zienkiewicz *et al.* [5] made an assessment of the suitability of the usage of the complete formulation depending on the frequency of the  
 20 loading and the permeability. The dynamic consolidation problems studied in that research were analyzed by Navas *et al.* [6] in the elastic range and also by López-Querol *et al.* [7] within the Generalized Plasticity model for small strains. Therefore, the extension of such formulation to a large deformation framework, within the  $u - w$  formulation, is an unquestionable  
 25 improvement in the field of the cyclic problems of saturated sands. Moreover, the employment of well known meshfree techniques is well indicated when large deformations are involved.

This paper is organized as follows: In chapter 2 the methodology is presented, being divided in four subsections where the  $u - w$  formulation, the  
 30 time integration scheme, the spatial discretization and the constitutive model are described; the model is calibrated in chapter 3, being analyzed the monotonic triaxial behavior under drained and undrained conditions test and the cyclic one in chapter 4 for both conditions also. Finally, conclusions are presented in chapter 5.

35 **2. Methodology**

*2.1. The  $u - w$  formulation*

The main idea of this formulation is the employment of the displacement of the solid and the relative displacement of the fluid as nodal variables. In the literature [8]  $\mathbf{u}^{ws}$ , the relative motion of the fluid with respect to the solid, is defined as  $(\mathbf{U} - \mathbf{u})$ , where  $\mathbf{u}$  and  $\mathbf{U}$  respectively stand for displacement vectors of the solid skeleton and the absolute displacement of the fluid phase. The rearrangement of these two gives us the relative displacement of the fluid phase,  $\mathbf{w}$ , with respect to the solid skeleton through the porosity as follows [9],

$$\mathbf{w} = n(\mathbf{U} - \mathbf{u}). \quad (1)$$

being the porosity,  $n$  calculated as

$$n = \frac{V_h}{V_h + V_s}, \quad (2)$$

where  $V_h$  and  $V_s$  are the volumes of the voids and solid grains respectively. Note that in the current work, totally saturated porous medium is assumed, i.e.,  $V_h$  coincides with the water volume, which results in  $S_w$  equal to 1 [8]. Thus, similarly, the mixture density,  $\rho$ , is derived from the ones of the fluid and solid particles,  $\rho_w$  and  $\rho_s$ , as follows:

$$\rho = (1 - n)\rho_s + n\rho_w. \quad (3)$$

The mass balance equation of the liquid water phase in a isothermal totally saturated media, being compressible water and soil grains and constant the water density, yields [8]

$$\frac{\dot{p}_w}{Q} + \text{div } \dot{\mathbf{u}} + \text{div } \dot{\mathbf{w}} = 0. \quad (4)$$

$Q$  represents the volumetric compressibility of the mixture, taking into account that the solid grains are much less compressible than the porous skeleton, is expressed in terms of the bulk modulus of the solid grains,  $K_s$ , and the compressive modulus of the fluid phase (water),  $K_w$ , [10] i.e.,

$$Q = \left[ \frac{1 - n}{K_s} + \frac{n}{K_w} \right]^{-1}. \quad (5)$$

In the whole research, the employment of  $K_w = 1e4$  MPa,  $K_s = 1e36$  MPa,  $\rho_s = 2600 \text{ kg/m}^3$  and  $\rho_w = 1000 \text{ kg/m}^3$  has been considered. Equation (4) can be integrated over time to obtain the pore pressure as

$$p_w = -Q [\text{div}(\mathbf{u}) + \text{div}(\mathbf{w})] + p_{w_0}, \quad (6)$$

where  $p_{w_0}$  is the initial pore pressure.

On the other hand, Lewis and Schrefler [8] also give the linear momentum balance equation for the multiphase system under saturated conditions as the summation of the dynamic equations for the individual constituents relative to the solid.

$$\text{div} \boldsymbol{\sigma} - \rho \ddot{\mathbf{u}} - \rho_w \ddot{\mathbf{w}} + \rho \mathbf{g} = \mathbf{0}. \quad (7)$$

where, taking into account Terzaghi's effective stress theory [11], the total Cauchy stress tensor,  $\boldsymbol{\sigma}$  can be written in terms of the effective stress,  $\boldsymbol{\sigma}'$ , and the pore pressure,  $p_w$ , as follows:

$$\boldsymbol{\sigma}' = \boldsymbol{\sigma} + \alpha p_w \mathbf{I}, \quad (8)$$

where  $\mathbf{I}$  is the second order unit tensor.

Finally, the third Biot's equation is derived from the general form of Darcy's law for any fluid phase:

$$-\text{grad } p_w - \frac{\mu_w}{k} \dot{\mathbf{w}} + \rho_w \left( \mathbf{g} - \ddot{\mathbf{u}} - \frac{\ddot{\mathbf{w}}}{n} \right) = \mathbf{0}. \quad (9)$$

where  $\dot{\mathbf{w}}/n$  represents the relative velocity of the fluid, taking into account that  $\dot{\square}$  is the material time derivative of  $\square$  with respect to the solid;  $\ddot{\mathbf{u}}$  denotes the solid phase acceleration,  $\ddot{\mathbf{w}}/n$  is the relative acceleration of the fluid respect to the solid phase,  $\mathbf{g}$  represents the external acceleration vector,  $\mu_w$  denotes the dynamic viscosity of the water and  $\mathbf{k}$  is the intrinsic permeability tensor, which becomes a unit tensor multiplied by the scalar  $k$ , intrinsic permeability, when isotropic permeability is assumed.

Both linear momentum balance equations of the mixture and the fluid were presented by Zienkiewicz *et al.* [10] with the convective terms, which can be neglected in the present research as the vorticity is relatively small compared to the rest of the terms.

#### 2.1.1. The weak form of system equations for the $u - w$ formulation

The weak form of the system equations for the  $u - w$  formulation is obtained applying the principle of virtual displacements to the linear momentum equation of both the solid and fluid phases, Eqs. (9) and (7).

Taking  $\delta \mathbf{u}$  and  $\delta \mathbf{w}$  as the virtual displacement vector for the solid and fluid phase respectively, the weak form of the linear momentum balance equations, once the definition of the pore pressure,  $p_w$ , of the equation (6) is introduced in both Eqs. (7) and (9) and Green's Theorem is applied, yields:

$$\begin{aligned} & - \int_B \boldsymbol{\sigma}' : \text{grad}(\delta \mathbf{u}) \, dv - \int_B Q \text{div}(\mathbf{u}) \mathbf{I} : \text{grad}(\delta \mathbf{u}) \, dv - \int_B Q \text{div}(\mathbf{w}) \mathbf{I} : \text{grad}(\delta \mathbf{u}) \, dv \\ & + \int_B [-\rho \ddot{\mathbf{u}} - \rho_w \ddot{\mathbf{w}} + \rho \mathbf{g}] \cdot \delta \mathbf{u} \, dv + \int_{\delta B} \bar{\mathbf{t}} \cdot \delta \mathbf{u} \, ds = 0. \end{aligned} \quad (10)$$

$$\begin{aligned} & - \int_B Q \text{div}(\mathbf{u}) \text{div}(\delta \mathbf{w}) \, dv - \int_B Q \text{div}(\mathbf{w}) \text{div}(\delta \mathbf{w}) \, dv - \int_B \frac{\mu_w}{k} \dot{\mathbf{w}} \cdot \delta \mathbf{w} \, dv \\ & - \int_B \ddot{\mathbf{w}} \frac{\rho_w}{n} \cdot \delta \mathbf{w} \, dv + \int_B \rho_w (\mathbf{g} - \ddot{\mathbf{u}}) \cdot \delta \mathbf{w} \, dv - \int_{\delta B} \bar{\mathbf{t}}_w \cdot \delta \mathbf{w} \, ds = 0. \end{aligned} \quad (11)$$

where  $B$  is the volume of the spatial domain and  $\delta B$  the boundary where the traction  $\bar{\mathbf{t}}$  and  $\bar{\mathbf{t}}_w$ , both traction of the solid and fluid phase, are applied.

## 2.2. Implicit time integration scheme: Newton-Raphson algorithm

In the  $u - w$  formulation each node contains both solid and fluid degrees of freedom,  $\mathbf{u}$  and  $\mathbf{w}$ , whereas the pore pressure,  $p_w$  is not considered as a degree of freedom, being calculated at the material point employing Eq. (6), in contrast with the more traditional  $u - p_w$  formulation, where is considered directly as an additional nodal unknown. On the one hand, the imposition of impervious boundary conditions is a bit easier in the  $u - w$  meanwhile the initial conditions require an initial calculation of the relative displacement of the water,  $w$ , when an initial pore pressure is assumed. This calculation is further explained in Appendix A.

In the proposed study, an axisymmetric 2D configuration is employed in order to represent the triaxial tests. As a two-dimensional problem, the nodal unknowns can be written as:

$$\mathbf{u}^* = [u_x \quad u_y \quad w_x \quad w_y]^T.$$

After assembling the elementary matrices, the final system of equations can be simplified as

$$\mathbf{R}_{k+1} + \mathbf{C} \dot{\mathbf{u}}_{k+1} + \mathbf{M} \ddot{\mathbf{u}}_{k+1} = \mathbf{P}_{k+1}, \quad (12)$$

where  $\mathbf{R}$ ,  $\mathbf{C}$  and  $\mathbf{M}$  respectively denote the internal forces vector and damping and mass matrices, whereas  $\mathbf{P}$  is the external forces vector, which contains both gravity acceleration and external nodal forces.  $k + 1$  represents the current step.

In order to solve Eq. (12) in an implicit way, a traditional Newmark time integration scheme with  $\gamma = 0.6$  and  $\beta = 0.325$ . (suitable for dynamic problems [12]) is employed. Inserting this scheme into Eq. (12), the equations for the unknowns can be re-written as:

$$\begin{aligned} \mathbf{G}_{k+1} &= \mathbf{M} [\alpha_1 \Delta \mathbf{u}_{k+1} - \alpha_2 \dot{\mathbf{u}}_k - \alpha_3 \ddot{\mathbf{u}}_k] \\ &+ \mathbf{C} [\alpha_4 \Delta \mathbf{u}_{k+1} + \alpha_5 \dot{\mathbf{u}}_k + \alpha_6 \ddot{\mathbf{u}}_k] \\ &+ \mathbf{R}_{k+1} - \mathbf{P}_k - \Delta \mathbf{P}_{k+1} = \mathbf{0}, \end{aligned} \quad (13)$$

or in the compact form:

$$\begin{aligned} \mathbf{G}(\boldsymbol{\chi}, \boldsymbol{\eta}) &= \mathbf{0}, \\ \text{where } \boldsymbol{\chi} &= [\boldsymbol{\chi}^u, \boldsymbol{\chi}^w]^T \text{ is the deformation mapping} \\ \text{and } \boldsymbol{\eta} &= [\delta \mathbf{u}, \delta \mathbf{w}]^T, \Delta \mathbf{u}^* = [\Delta \mathbf{u}, \Delta \mathbf{w}]^T. \end{aligned} \quad (14)$$

where the  $\alpha$ -parameters are listed in Table 1 according to Wriggers [13]. These coefficients can be easily extended to any other time integration schemes.

Table 1: The  $\alpha$ -parameters of the Newmark scheme.

$$\begin{aligned}\alpha_1 &= \frac{1}{\beta \Delta t^2} & \alpha_2 &= \frac{1}{\beta \Delta t} & \alpha_3 &= \frac{1}{2\beta} - 1 \\ \alpha_4 &= \frac{\gamma}{\beta \Delta t} & \alpha_5 &= 1 - \frac{\gamma}{\beta} & \alpha_6 &= \left(1 - \frac{\gamma}{2\beta}\right) \Delta t\end{aligned}$$

According to Wriggers [13], to solve the above non-linear equations, any Newton method can be applied by using the following statement, after the  
85 linearization of  $\chi$ :

$$\mathbf{G}(\bar{\chi}, \boldsymbol{\eta})_{k+1}^i + D\mathbf{G}(\bar{\chi}, \boldsymbol{\eta})_{k+1}^i \cdot \Delta \mathbf{u}_{k+1}^{*i+1} \cong \mathbf{0}, \quad (15)$$

where  $\bar{\chi}$  is the already linearized deformation mapping. Thus, the iterative procedure, taking into account the matrices that are involved in our problem, yields:

$$\begin{aligned}[\alpha_1 \mathbf{M} + \alpha_4 \mathbf{C} + \mathbf{K}_{k+1}^i] \Delta \mathbf{u}_{k+1}^{i+1} &= -\mathbf{G}(\mathbf{u}_{k+1}^i), \\ \text{where } \mathbf{u}_{k+1}^{i+1} &= \mathbf{u}_{k+1}^i + \Delta \mathbf{u}_{k+1}^{i+1}.\end{aligned} \quad (16)$$

where  $\mathbf{K}$  is the tangential stiffness matrix:

$$\mathbf{K}(\mathbf{u}_{k+1}^i) = \mathbf{K}_{k+1}^i = \left. \frac{\partial \mathbf{R}}{\partial \mathbf{u}} \right|_{\mathbf{u}_{k+1}^i}. \quad (17)$$

and  $i$  depicts the iteration index. The iteration finishes when  $\mathbf{G}_{k+1}^i$  is lower  
90 than a given tolerance.

After applying the integration in time, Eq. (10) and Eq. (11) are written at time  $t_{k+1}$  and transformed as follows:

$$\begin{aligned}& - \int_B \boldsymbol{\sigma}' : \text{grad}(\delta \mathbf{u}) dv - \int_B Q \text{div}(\mathbf{u}) \text{div}(\delta \mathbf{u}) dv \\& - \int_B Q \text{div}(\mathbf{w}) \text{div}(\delta \mathbf{u}) dv - \alpha_1 \int_B [\rho \mathbf{u} + \rho_w \mathbf{w}] \cdot \delta \mathbf{u} dv \\& + \int_B \rho \mathbf{g} \cdot \delta \mathbf{u} dv + \alpha_8 \int_{\delta B} \bar{\mathbf{t}} \cdot \delta \mathbf{u} ds = \mathbf{0}\end{aligned} \quad (18)$$

$$\begin{aligned}& - \int_B Q \text{div}(\mathbf{u}) \text{div}(\delta \mathbf{w}) dv - \int_B Q \text{div}(\mathbf{w}) \text{div}(\delta \mathbf{w}) dv \\& - \alpha_4 \int_B \frac{\mu_w}{k} \mathbf{w} \cdot \delta \mathbf{w} dv - \alpha_1 \int_B \frac{\rho_w}{n} \mathbf{w} \cdot \delta \mathbf{w} dv \\& - \alpha_1 \int_B \rho_w \mathbf{u} \cdot \delta \mathbf{w} dv + \int_B \rho_w \mathbf{g} \cdot \delta \mathbf{w} dv \\& - \int_{\delta B} \bar{\mathbf{t}}_w \cdot \delta \mathbf{w} ds = \mathbf{0}.\end{aligned} \quad (19)$$

The results of the linearization process for Eq. (18) and Eq.(19) are given in Eq. (Appendix B.1) and Eq. (Appendix B.2) respectively in Appendix B. More details of the linearization process are given in [14].

### 2.3. Spatial discretization

The shape function employed is based that of Arroyo and Ortiz [15], who defined exponential functions based on the principle of the local maximum entropy (LME). For a node  $a$ , it reads,

$$N_a(\mathbf{x}) = \frac{\exp[-\beta |\mathbf{x} - \mathbf{x}_a|^2 + \boldsymbol{\lambda}^* \cdot (\mathbf{x} - \mathbf{x}_a)]}{Z(\mathbf{x}, \boldsymbol{\lambda}^*(\mathbf{x}))}, \quad (20)$$

where

$$Z(\mathbf{x}, \boldsymbol{\lambda}) = \sum_{a=1}^{N_b} \exp[-\beta |\mathbf{x} - \mathbf{x}_a|^2 + \boldsymbol{\lambda} \cdot (\mathbf{x} - \mathbf{x}_a)]. \quad (21)$$

$N_b$  represents the neighborhood size. The parameter  $\beta$  defines the shape of the neighborhood and  $\boldsymbol{\lambda}^*(\mathbf{x})$  comes from the minimization of the function  $g(\boldsymbol{\lambda}) = \log Z(\mathbf{x}, \boldsymbol{\lambda})$  to guarantee the maximum entropy. The first derivatives of the shape function are then obtained from differentiating the shape function itself to get the Hessian matrix  $\mathbf{J}$  in the following expression:

$$\nabla N_a^* = -N_a^* (\mathbf{J}^*)^{-1} (\mathbf{x} - \mathbf{x}_a). \quad (22)$$

A modified Nelder-Mead algorithm developed by Navas *et al.* [16] is used for the minimization process in the current work.

### 2.4. Hyperelasto-plastic material model: the Generalized Plasticity

As it was mentioned, the main contribution of this work in the sense of the constitutive model is the implementation of the Generalized Plasticity flow within a large deformation framework. This scheme employs as the main strain measurement the deformation gradient tensor, calculated in an incremental way thanks to the updated lagrangian approach (CITAS, CITAS). For both phases, the increments are calculated with the gradient of the Local Max-Ent shape functions, Eq. (22), as follows:

$$\Delta \mathbf{F}_{k+1} = \mathbf{I} + \sum_{a=1}^{N_b} \Delta u_{k+1}^a \nabla N^a(x_k^p), \quad (23)$$

$$\Delta \mathbf{F}_{k+1}^w = \mathbf{I} + \sum_{a=1}^{N_b} \Delta w_{k+1}^a \nabla N^a(x_k^p) \quad (24)$$

where the superscript  $p$  represents the material point where is calculated and  $Nb$  the neighbor nodes of this material point. The deformation gradient can be calculated as:

$$\mathbf{F}_{k+1} = \Delta \mathbf{F}_{k+1} \mathbf{F}_k \quad (25)$$

where  $k$  and  $k + 1$  depict the previous and the current step.

The methodology that is employed in this research reproduces the proposed by Navas *et al.* [14] for the pore pressure and stress update: following the work of Cuitiño and Ortiz [17] to relate the left Cauchy-Green strain tensor  $\mathbf{B}$  and the small strain tensor  $\boldsymbol{\varepsilon}$  during the trial step, where  $\mathbf{B} = \mathbf{F}\mathbf{F}^T$ . Following, the main relationships between large and small strain configurations that are employed herein are presented.

$$\boldsymbol{\varepsilon}_{k+1}^{e\,trial} = \frac{1}{2} \log \mathbf{B}_{k+1}^{e\,trial}, \quad (26)$$

$$\text{div}(\mathbf{u}) = \text{tr}(\boldsymbol{\varepsilon}_{k+1}) = \text{tr}\left(\frac{1}{2} \log \mathbf{B}_{k+1}\right), \quad (27)$$

$$\text{div}(\mathbf{w}) = \text{tr}(\boldsymbol{\varepsilon}_{k+1}^w) = \text{tr}\left(\frac{1}{2} \log \mathbf{B}_{k+1}^w\right), \quad (28)$$

$$p_w = -Q(\text{div} \mathbf{u} + \text{div} \mathbf{w}). \quad (29)$$

One interesting issue of Constitutive laws in soils is its definition by means of  $p'$ ,  $q$  and  $\theta$  stress components, which are defined as follows:

$$p' = -\frac{1}{3}I_1 \quad (30)$$

$$q = (3J_2)^{1/2} \quad (31)$$

$$\theta = \frac{1}{3} \sin^{-1} \left( \frac{-3\sqrt{3}}{2} \frac{J_3}{J_2^{3/2}} \right) \quad (32)$$

where  $I_1$ ,  $J_2$  and  $J_3$ , respectively, denote the first invariant of effective stress tensor and second and third invariants of deviatoric stress tensor. Negative sign in Equation (30) stands for positive values of  $p'$  in compression. However, the sign of  $q$  is closely related to the orientation in the triaxial space, *i.e.*, the Lode's angle  $\theta$  of the stress path: if  $\sin 3\theta$  is lower than 0, we consider the load in tension and the sign of  $q$  negative, meanwhile  $q$  is positive on any other situation. Working with  $p$  and  $q$  is an aspect that allows as to reduce the computational effort since only two variables define the stress state of the material point instead of every component of the stress tensor in the cartesian space as it was the traditional way to operate with Generalized



Plasticity [2].

135 In the same manner, strains can be defined in the triaxial space taking into account again that the sign of  $\varepsilon_s$  will be defined be a conjugate strain Lode's angle. The expressions read as follows:

$$\varepsilon_v = -tr(\boldsymbol{\varepsilon}) \quad (33)$$

$$\varepsilon_s = \sqrt{\frac{2}{3}} \|\boldsymbol{\varepsilon}^{dev}\| \quad (34)$$

$$\theta^\varepsilon = \frac{1}{3} \sin^{-1} \left( \frac{-3\sqrt{3}}{2} \frac{J_3^\varepsilon}{J_2^{\varepsilon^{3/2}}} \right) \quad (35)$$

In this work, the hyperelastic HAR model [18] has been employed, with the reduced version ( $n = 1$ ). The Free Energy function is represented by the following equation:

$$\psi(\varepsilon_v^e, \varepsilon_s^e) = \frac{p_a}{K_0} \cdot \exp \left( K_0 \cdot \varepsilon_v^e + \frac{3G_0K_0(\varepsilon_s^e)^2}{2} \right) \quad (36)$$

Invariants  $p$  and  $q$  can be calculated from this function taking into account their own derivatives with respect to the strain invariants  $\varepsilon_v^e$  and  $\varepsilon_s^e$ :

$$\begin{bmatrix} p \\ q \end{bmatrix} = \begin{bmatrix} \frac{\partial^2 \psi}{\partial \varepsilon_v^e{}^2} & \frac{\partial^2 \psi}{\partial \varepsilon_v^e \partial \varepsilon_s^e} \\ \frac{\partial^2 \psi}{\partial \varepsilon_s^e \partial \varepsilon_v^e} & \frac{\partial^2 \psi}{\partial \varepsilon_s^e{}^2} \end{bmatrix} \begin{bmatrix} \varepsilon_v^e \\ \varepsilon_s^e \end{bmatrix} \quad (37)$$

140 Once defined the hyperelastic part, the plastic behavior is described only with the normal vectors to the yield and the potential surfaces, given respectively by  $n$  and  $n_g$ . The potential vector take different direction depending on the loading or unloading criteria. In the  $p, q, \theta$  stress space, these vectors are:

$$n = (n^p, n^q, n^\theta)^T \quad (38)$$

$$n_{g,L} = (n_{g,L}^p, n_{g,L}^q, n_{g,L}^\theta)^T \quad (39)$$

$$n_{g,U} = (n_{g,U}^p, n_{g,U}^q, n_{g,U}^\theta)^T \quad (40)$$

where the components are described in Table 2.

Table 2:  $n_g$  and  $n$  components.

$$\left. \begin{aligned} n^p &= \frac{d_f}{\sqrt{1+d_f^2}} \\ n^q &= \frac{\pm 1}{\sqrt{1+d_f^2}} \\ n^\theta &= -\frac{qM_f \cos 3\theta}{2\sqrt{1+d_f^2}} \end{aligned} \right| \left. \begin{aligned} n_{g,L}^p &= \frac{d_g}{\sqrt{1+d_g^2}} \\ n_{g,U}^p &= -\|n_{g,L}^p\| \\ n_{g,L}^q &= \frac{\pm 1}{\sqrt{1+d_g^2}} \\ n_{g,L}^\theta &= -\frac{qM_g \cos 3\theta}{2\sqrt{1+d_g^2}} \end{aligned} \right.$$

145 The dilatancies are represented by  $d_f = (1 + \alpha_f)(M_f - \eta)$  and  $d_g =$   
 $(1 + \alpha_g)(M_g - \eta)$ , taking into account that  $M_g$  and  $M_f$  are the slopes of the  
critical state lines of the potential and yield surfaces respectively and  $\alpha_g$  and  
 $\alpha_f$  are model parameters.  $\eta$  depicts the current relation between  $q/p$ . As we  
see in Table 1, the deviatoric component can take positive or negative sign,  
150 which depends on the sign of the invariant  $q$ , if it is in extension (negative)  
or compression (positive).

The goal of the plastic driver is the calculation of the plastic part of the  
strain tensor. In the Generalized Plasticity, it can be calculated as:

$$d\boldsymbol{\varepsilon}^p = \frac{1}{H_{L/U}} (\mathbf{n}_{gL/U} \otimes \mathbf{n}) : d\boldsymbol{\sigma} \quad (41)$$

Although this assertion is valid for any space, in our case,  $d\boldsymbol{\sigma}$  and  $d\boldsymbol{\varepsilon}^p$  are  
defined in the triaxial space. On the other hand,  $H_{L/U}$  is called the plastic  
modulus, which is defined in a different way depending on the loading or  
unloading conditions. In the first case it is plotted as:

$$H = p H_0 H_f (H_v + H_s) H_{DM} \quad (42)$$

where  $H_0$  is a material parameter that Schrefler and coworkers [19] related  
to the traditional slopes of the plastic and elastic curves in the  $p - e$  curve:

$$H_0 = \frac{1 + e_0}{\lambda - k} = \frac{1}{\lambda^* - k^*} \quad (43)$$

The rest of the parameters are defined following:

$$\begin{aligned} H_f &= \left(1 - \frac{\eta}{\eta_f}\right)^4 \\ H_v &= (1 - \eta/M_g) \\ H_s &= \beta_0 \beta_1 \exp(-\beta_0 \xi) \\ H_{DM} &= \left(\frac{\zeta_{\max}}{\zeta}\right)^{\gamma_{DM}} \end{aligned} \quad (44)$$

where:

$$\begin{aligned} \eta_f &= \left(1 + \frac{1}{\alpha_f}\right) M_f \\ \zeta &= p' \left\{1 - \left(\frac{\alpha_g}{1 + \alpha_g}\right) \frac{\eta}{M_g}\right\}^{-1/\alpha_g} \end{aligned} \quad (45)$$

$\zeta_{\max}$  is the maximum value of  $\zeta$  along the computation and  $\xi$  is the cumulative  
deviatoric plastic strain,  $\int |d\boldsymbol{\varepsilon}_s^p|$ . On the other hand, if the process lies on the

unloading,  $H$  must follow the following equations, depending on the relation  $\left| \frac{M_g}{\eta_u} \right|$ , being  $\eta_u$  the value of  $\eta$  in the turning point (loading to unloading):

$$\begin{aligned} H_U &= H_{U0} \left( \frac{M_g}{\eta_u} \right)^{\gamma_u} & \text{if } \left| \frac{M_g}{\eta_u} \right| > 1 \\ H_U &= H_{U0} & \text{if } \left| \frac{M_g}{\eta_u} \right| \leq 1 \end{aligned} \quad (46)$$

Once the plastic part is solved, strain and stress tensor, in finite deformation, have to be calculated:

$$\boldsymbol{\sigma} = \frac{1}{J} \boldsymbol{\tau} = \frac{1}{J} \left( p \mathbf{I} + \sqrt{\frac{2}{3}} q n_{k+1}^{tr} \right) \quad (47)$$

$$\mathbf{B}^e = \exp(\boldsymbol{\varepsilon}_{k+1}^e) = \exp \left( \frac{1}{3} \varepsilon_v^e \mathbf{I} + \sqrt{\frac{3}{2}} \varepsilon_s^e n_{k+1}^{tr} \right) \quad (48)$$

In the above equations,  $\mathbf{I}$  is the identity matrix and  $\mathbf{n}_{k+1}^{tr}$  is the normalized unit tensor of the trial deviatoric elastic strain tensor,  $\boldsymbol{\varepsilon}_{k+1}^{tr,e}$ , i.e.,

$$\mathbf{n}_{k+1}^{tr} = \frac{\boldsymbol{\varepsilon}_{k+1}^{tr,e}}{\|\boldsymbol{\varepsilon}_{k+1}^{tr,e}\|}. \quad (49)$$

Finally, since the presented procedure presents an implicit time integration scheme, the consistent tangent modulus is obtained by:

$$\mathbf{D}^{ep} = \mathbf{D}^e - \frac{(\mathbf{D}^e n_g)(n \mathbf{D}^e)}{H + n^T \mathbf{D}^e n_g} \quad (50)$$

where  $n_g$  and  $n$  have to be converted to the cartesian space and  $\mathbf{D}^e$  is the consistent tangent moduli of the elastic part, calculated, also in cartesian, by:

$$\begin{aligned} \mathbf{D}^e &= D_{11}^e \mathbf{I} \otimes \mathbf{I} + \sqrt{\frac{2}{3}} D_{12}^e \mathbf{I} \otimes \hat{\mathbf{n}} + \sqrt{\frac{2}{3}} D_{21}^e \hat{\mathbf{n}} \otimes \mathbf{I} \\ &+ \frac{2q}{3\varepsilon_s^e} \mathbf{M}_1 + \frac{2}{3} \left( D_{22}^e - \frac{q}{\varepsilon_s^e} \right) \hat{\mathbf{n}} \otimes \hat{\mathbf{n}} \end{aligned} \quad (51)$$

being  $D_{\square\square}^e$  the components of the elastic matrix in the triaxial space, Eq. (37), and  $\mathbf{M}_1$  the matrix that relates the total and the deviatoric strain tensors in Voigt notation ( $\mathbf{M}_1 \boldsymbol{\varepsilon} = \boldsymbol{\varepsilon}^{dev}$ ), which is constructed in the following manner:

$$\mathbf{M}_1 = \mathbf{1} - \frac{1}{3} (\mathbf{I} \otimes \mathbf{I}) \quad (52)$$

where  $\mathbf{1}$  is the fourth order identity matrix.

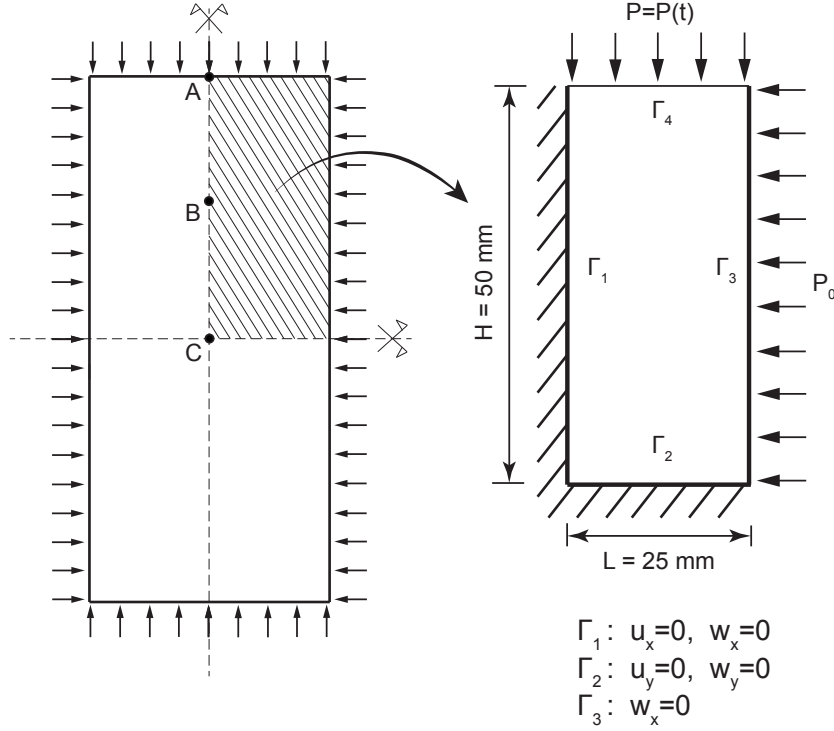


Figure 1: Scheme of the geometry employed in the triaxial test modeling.

### 3. Model calibration

The calibration consist of the simulation of several tests, under monotonic loading conditions, of a determined soil, comparing to reference undrained results. For the drained part, the goal is discovering the drainage velocity, being also analyzed the behavior of the soil under drained triaxial conditions. These three results are presented following.

#### 3.1. Monotonic triaxial test: undrained conditions

The proposed methodology has to be validated first. A triaxial test with dynamic conditions is proposed since there are several results of this kind of test in literature [1, 10]. In Fig. 1 a scheme of this test is presented. Because of the symmetry only one quarter of its geometry can be modeled. Thus, boundaries  $\Gamma_1$  and  $\Gamma_2$  have to constraint the displacement of the solid and fluid in the perpendicular direction. Boundary  $\Gamma_3$  is free to move, although the fluid cannot dissipate in that boundary since there is a membrane to avoid it.

Boundary  $\Gamma_4$  will change depending on the problem to be modeled. About the soil, either the displacement can be imposed or the pressure, if we want

Table 3: Material properties employed in the different studied problems.  $\alpha_f = \alpha_g = 0.45$

	3.1 A	3.1 B	3.1 C	3.1 D	3.2-3.3	4.1-1	4.1-2	4.2
$K_0$ [MPa]	35	35	35	35	35	35	65	
$G_0$ [MPa]	52.5	52.5	52.5	52.5	65	52.5	30	
$M_f$	0.4	0.545	0.57	0.72	0.5	0.4	0.71	
$M_g$	1.5	1.32	1.12	1.03	1.03	1.5	1.5	
$H_0$	350	350	350	350	350	350	800	
$\beta_0$	4.2	4.2	4.2	4.2	4.2	4.2	3.8	
$\beta_1$	0.2	0.2	0.2	0.2	0.2	0.2	0.16	
$\gamma$	-	-	-	-	-	4	1	
$H_{u0}$	-	-	-	-	-	600	250	
$\gamma_u$	-	-	-	-	2	5		

175 to reach a desire value of the  $q$ . On the other hand, the impermeability of this boundary will be given due to the drained or undrained condition of the reproduced test.

The first test to validate is an undrained monotonic test. The material employed within these tests was a sand studied by Castro (CITA) that, afterwards, was calibrated for the Generalized Plasticity model [1, 10]. The 180 parameters that were calibrated are presented in Table 3. Four different sands are studied, depending on the density state.

In this validation test boundary  $\Gamma_4$  is impermeable, what makes the experiment undrained. The soil is deformed until around 8 %, which can be considered a considerable deformable range. In Fig. 2 the obtained results are depicted. The left image shows the comparison between the theoretical results proposed by Pastor *et al.* [1] for the different results of the deviatoric stress against the ones obtained with the proposed methodology, observing very good agreement for the 4 studied soils. This agreement is also achieved 190 in the stress paths (right column).

### 3.2. Monotonic consolidation test

Once the behavior of the constitutive model is validated, it is time to verify the performance of the Biot's formulation when the displacement of the water comes into place. Thus, an oedometer, with the geometry proposed in Fig. 1, is simulated in order to check the consolidation time. A permeability 195 of  $1e-6$  m/s and a porosity of 0.43 are employed within this simulation. A pressure of 200 kPa is applied to the soil during 0.05 s, point that we consider the consolidation starts. The settlement is obtained from the beginning of the process. The first second of the simulation is presented in Fig. 3 for both 200 pore pressure and settlement.

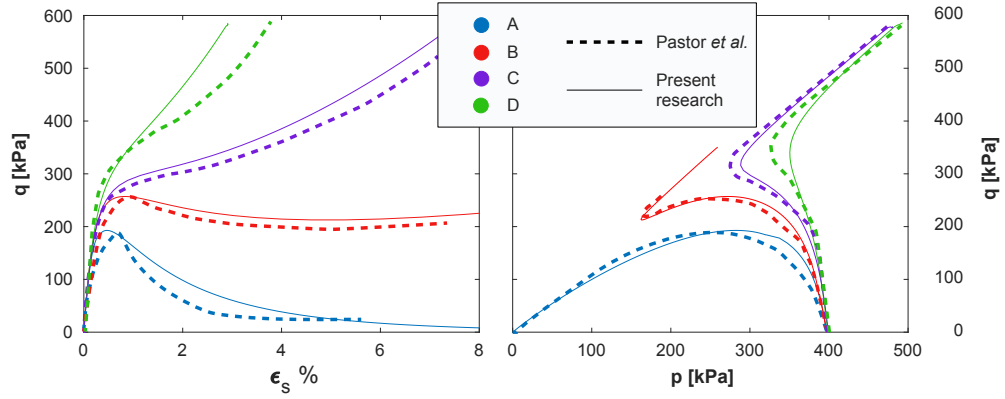


Figure 2: Comparison between the results of the undrained triaxial test for the 4 different studied soils obtained by Pastor *et al.* [1] and with the proposed methodology: stress-strain (left) and stress path (right).

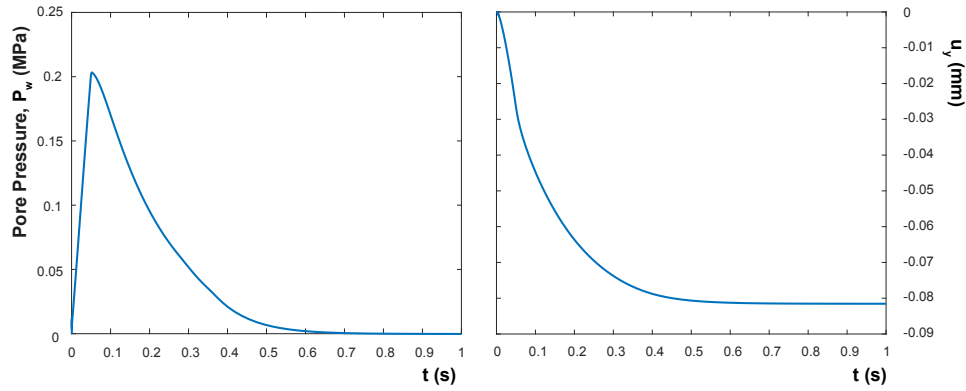


Figure 3: Consolidation results: a) Pore pressure, b) Settlement.

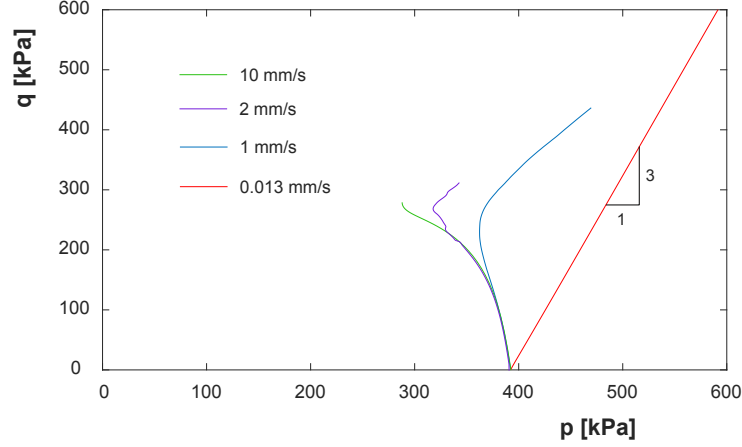


Figure 4: Stress path of the monotonic triaxial tests under drained conditions for different loading rates.

Experimentally, it is demonstrated that the maximum strain rate to obtain drained conditions in a drained triaxial test can be obtained with the following equation:

$$v_{load} = \frac{\varepsilon_f H}{12.7 t_{100}} \quad (53)$$

where  $\varepsilon_f H$  is a measurement of the shortening of the specimen and  $t_{100}$  is the consolidation time. Since 100% is not possible to be reached, a 95 % of the dissipation of the pore pressure has been considered, which in Fig. 3 is observed to be around 0.48 s. Since the shortening is 0.08 mm, the velocity in which the whole specimen is able to dissipate all the excess pore water pressure has to be slower than 0.013 mm/s.

### 3.3. Monotonic triaxial test: drained conditions

The last monotonic test goes deeper in the drained conditions. Once the velocity to get drained conditions is calculated, a drained triaxial test with the same soil parameters of the previous section is simulated. The boundary  $\Gamma_4$  of Fig. 1 in this case allows the water outlet. Thus, the point to study if the drainage is reached if a loading rate of 0.013 mm/s is employed will be the one farther than the boundary  $\Gamma_4$ , *i.e.* point C of Fig. 1. The obtained stress path in that point is depicted in Fig. 4. We can see that, in this point, an slope 3:1, typical of drained triaxial tests, is obtained for that velocity, corroborating the hypothesis of equation (3.2).

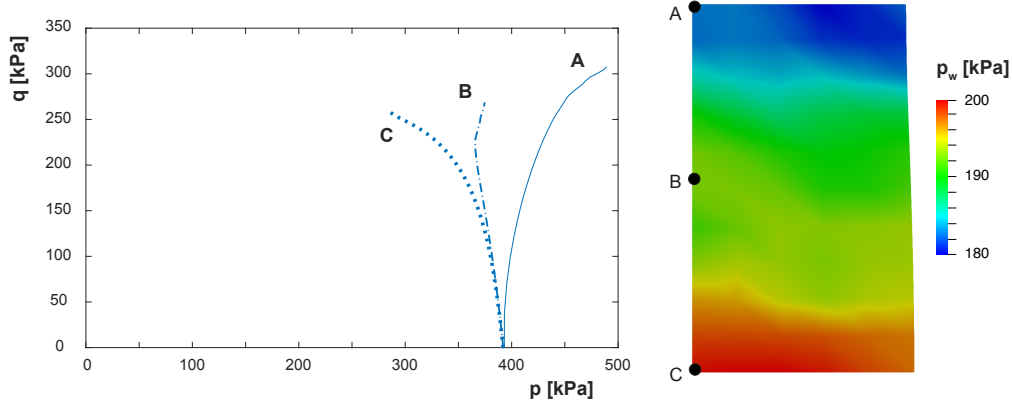


Figure 5: a) Stress path of the monotonic triaxial tests under drained conditions for a loading rate of 10 mm/s at three different locations, b) Pore pressure distribution at 1.5 % of axial strain and location of different control locations.

Some faster loading velocities are studied also. The stress paths for that loading rates cover a range between the slope 3:1 and the stress path of 10 mm/s. We have seen the stress path is related to the relative density, which is function of the relationship  $M_f/M_g$ . This ratio, for the studied soil, is 0.49, which is similar to ratio of soil C of section 3.1. Thus, the stress path for undrained conditions is similar, what makes us think that, for 10 mm/s (or faster) in the middle of the specimen undrained conditions are obtained. For different locations, different paths are obtained. In Fig. 5, the stress paths of locations A, B and C are plotted. The closer is the boundary  $\Gamma_4$ , the more drained is the behavior and the the stress path tends to seek the slope 3:1. However, there is not total drainage in point A. The reason is the excess of pore water pressure generated when the loading velocity is high. In Fig. 5 the distribution of pore pressure along the specimen when the 1.5 % of the strain is reached is depicted also.

Finally, the pore pressure generated depending on the loading rate is assessed. In Fig. 6 the pore pressure at point C when 1.5 % of the strain is reached for different loading rates is plotted. Obviously, the dissipation is low when the loading rate increases.

#### 4. Cyclic triaxial test

The Generalized Plasticity model is well-known in the modeling of cyclic behavior since, explicitly, the stress state is incorporated to the yield and potential surface normal vectors. In the proposed methodology, the trend is captured in advance by the  $\theta$  angle of the strain state. The good performance



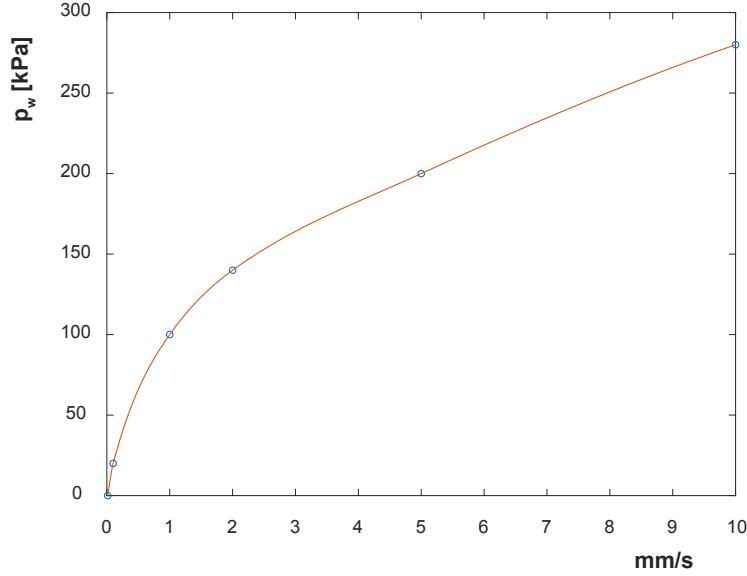


Figure 6: Pore pressure at point C when 1.5 % of the strain is reached for different loading rates.

of the proposed methodology is verified following with the simulated drained  
245 and undrained triaxial tests.

#### 4.1. Undrained conditions

This test is simulated with the same Dirichlet boundary conditions that the ones employed in Section 3.1. Two loading conditions are studied, being those that were previously studied theoretically by Pastor *et al.* [1].

250 The first only lies on the compression range, studying the loading-unloading cycle. The soil parameters are presented in Table 3, column 4.1-1. The results fit very well with the proposed in the studied bibliography. They can be observed in Fig. 7.

The problem shows that, after several cycles, the soil loses the initial  
255 stiffness due to the liquefaction induced by the cyclic loading. Thus, the strain increases dramatically and there is a reduction of the solid pressure. If we study the pore water pressure, depicted in Fig. 8, we can observe an important increasing at the same time that the stiffness decrease, confirming the liquefaction process.

260 On the other hand, in the second test the whole cycle is assessed, *i.e.* compression loading, compression unloading, tension loading, tension unloading. A different soil from the previous test is employed, being the parameters shown in Table 3, column 4.1-2. The obtained stress path is plotted in

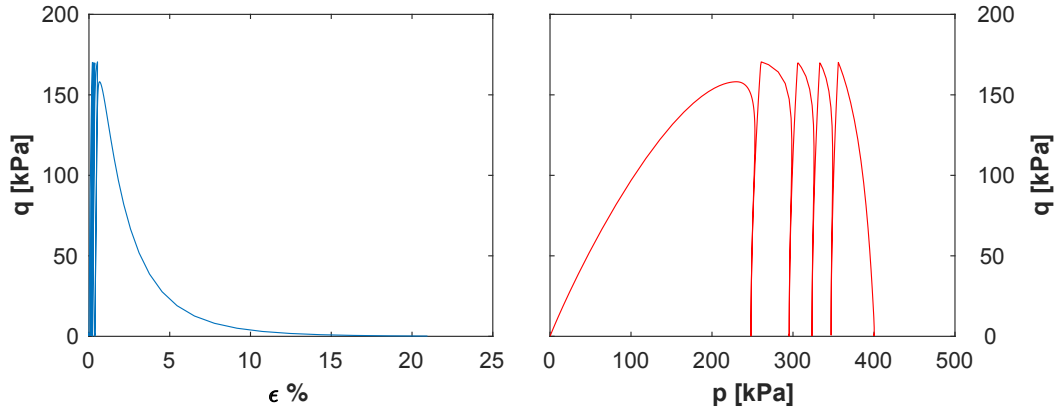


Figure 7: Results of the cyclic triaxial tests under undrained conditions: compression.

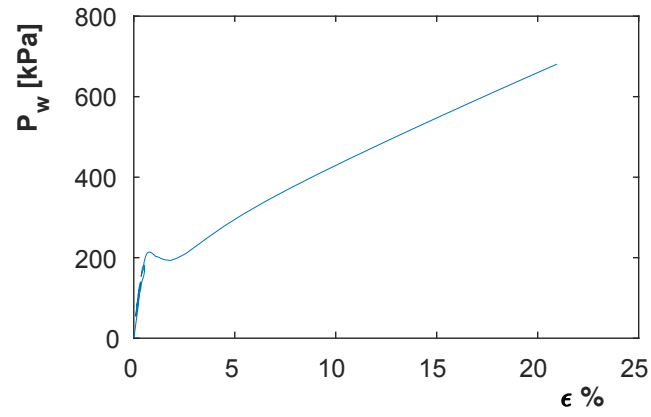


Figure 8: Pore water pressure results of the cyclic triaxial tests under undrained conditions: compression.

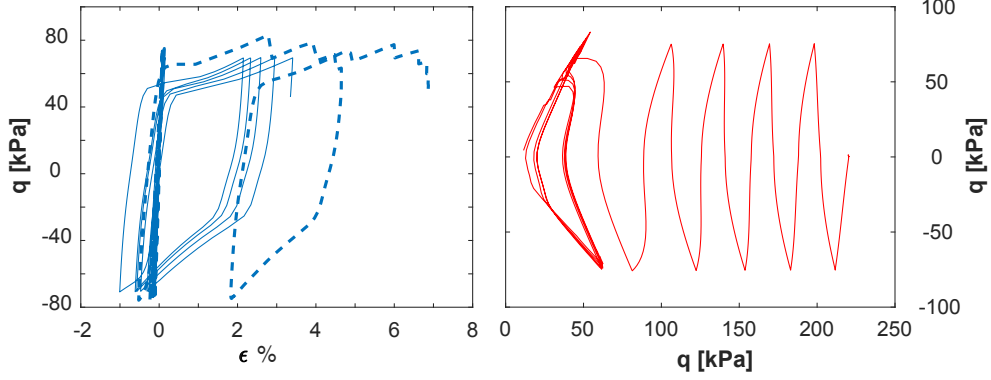


Figure 9: Results of the cyclic triaxial tests under undrained conditions: tension-compression.

Fig. 9.B, which is equivalent to the obtained by Pastor *et al.* [1]. This path is  
 265 obtained independently to the loading rate. However, the stress-deformation  
 curve is dependent on the loading rate, as it is observed in Fig. 9.A. In dashed  
 line it is plotted the curve obtained by increasing the angular frequency. **The  
 reason can be that the excess pore water pressure generated, when the phone-  
 mana is quick, cannot be stabilized and provoke a liquefaction of the material  
 270 that enlarges the strain.**

#### 4.2. Drained conditions

The typical behavior that is seen when drained conditions are imposed in  
 the triaxial test shows a densification. However, the proposed material model  
 is unable to reproduce this behavior without multiplying to  $H$ , Eq. (2.4), the  
 term  $H_d$ , a densification measurement, which is calculated as follows:

$$H_d = \exp(-\gamma_d \varepsilon_v^p) \quad (54)$$

where  $\varepsilon_v^p$  is the cumulative volumetric plastic strain and  $\gamma_d$  is a material  
 parameter, which is employed in this research as 400. The higher is this  
 parameter, the quicker the densification is obtained. This technique was  
 275 proposed by Zienkiewicz and coworkers [10].

The test consist of varying the deviatoric load between 300 kPa and 150  
 kPa, what gives us a variation of  $\eta = p/q$ , of around 0.2 and -0.2. The em-  
 ployed parameters are given in TABLE XXX. In Fig. 10 the results with and  
 without the employment of the densification parameter, which is equivalent  
 280 to employ  $\gamma_d = 0$ , are depicted. The goal is the reproduction of the typi-  
 cal behavior shown in drained sands, already presented by Bahda [20] and  
 Zienkiewicz and coworkers [10].

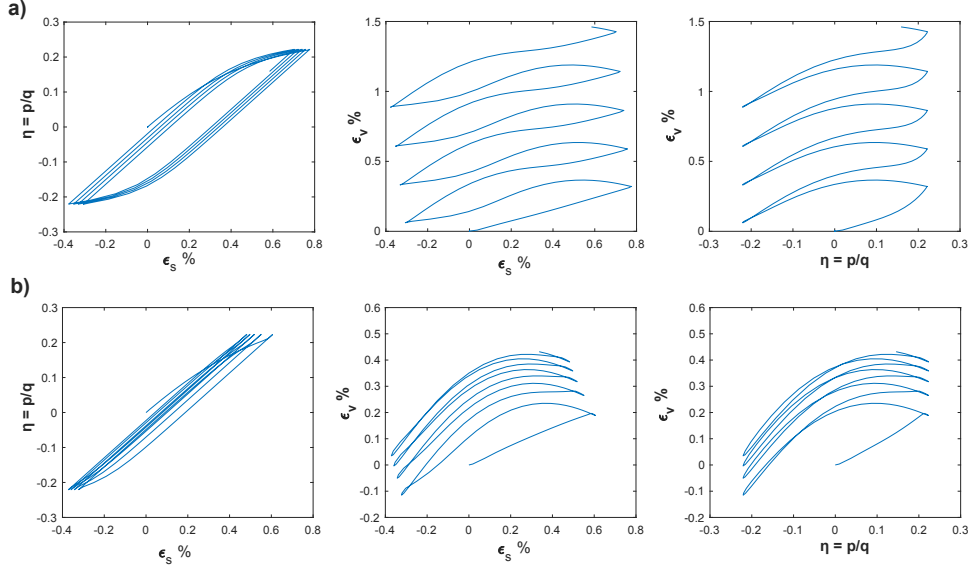


Figure 10: Results of the cyclic triaxial tests under drained conditions without, a), and with, b), the densification parameter  $Hd$ .

In the first row of the Fig. 10 the results without densification are presented. It can be seen how there is an increasing of the volumetric strain with the increasing of the numbers of cycles of loading. However, the increment of volumetric strain is equal in every cycle, not observing any hardening of the material, which is not the sought behavior. Thus, in the second row, we can observe how the increment of  $\varepsilon_v$  is reduced in every cycle, since while the  $\varepsilon_v^p$  increases, the value of  $H$  and, therefore, the stiffness of the material, grows. After the same number of cycles, a lower value of  $\varepsilon_v$  is obtained.

## 5. Conclusions

An interesting methodology to model the dynamic behavior of saturated sands within large deformation is proposed in this paper. Several tools are collected in order to reach the sought behavior of the soil. First of all, the complete  $u - w$  large strain formulation developed within an implicit time integration scheme helps us to model the dynamic behavior of saturated sands. Previously, this methodology was proposed with the Optimal Transportation Meshfree with excellent results [14]. Finally, the Generalized Plasticity is well-known to capture properly the behavior of this soil when cyclic loads are involved. However, it was necessary to adapt this model to work in the large deformation framework, which is a big novelty of this work.

The results show excellent performance of the aforementioned tools. Different behaviors were studied in order to assess the suitability of the proposed methodology. The first one, the undrained monotonic one, help us to validate the proposed constitutive model successfully. Following, the limit of the drained-undrained condition is analyzed for the proposed soil and, in chapter 4, the behavior of the model under drained conditions is assessed, verifying that, when the relative motion of the water is not negligible the  $u - w$  formulation presents good results. In chapter 5 we could observe the performance of the method under cyclic loads, obtaining the expected behaviors: liquefaction in undrained and densification in drained tests.

The good results obtained in this research encourage us to extend this work in several directions. First of all, since only triaxial tests were carried out, more sophisticated experimental tests as well as real field cases have to be studied with the proposed methodology. On the other hand, several improvements can be made to the constitutive model. The density of the sand in chapter 3 was a relationship between  $M_f$  and  $M_g$ , meanwhile recent developments of the Generalized Plasticity proposed by Manzanal *et al.* [3, 4] made the densification process in the Generalized Plasticity model more elegant, being able to reproduce the behavior of the soil of the chapter 5.2 easily. Finally, as the methodology is able to capture dynamic behavior, makes sense that the constitutive model were able to capture different behaviors depending on the loading rate with some viscoplastic adjustment, which is something hardly explored within this model.

## Acknowledgements

The financial support to develop this research from the *Ministerio de Ciencia e Innovación*, under Grant Number, BIA-XXXXX is greatly appreciated. The first author also acknowledges the fellowship Juan de la Cierva FJCI-2017-31544.

## 330 Appendix A. Initial conditions in the $u - w$ formulation

Some of the triaxial test have, as starting points, initial stress states. In the Generalized Plasticity, it is also necessary to provide this state. Indeed, the stress of this initial point comes from a strain state. The Updated Lagrangian configuration employed within this research needs the previous Deformation Gradient and the current increment in order to situate in the current state. Thus, for the first step we need the tensor  $\mathbf{F}$  of the initial state. Since no tangential stress takes place we can assume:

$$\mathbf{F}_{ij} = \exp \boldsymbol{\varepsilon}_{ij} \quad (\text{Appendix A.1})$$

where  $\boldsymbol{\varepsilon}_{ij}$  comes from the iterative calculation:

$$\boldsymbol{\varepsilon}_{ij} = \mathbf{D}_{ijkl}^{-1}(\boldsymbol{\varepsilon}_{ij}) \boldsymbol{\sigma}_{ij}(\boldsymbol{\varepsilon}_{ij}) \quad (\text{Appendix A.2})$$

The imposition of the initial pore pressure in the  $u - w$  formulation is not so straightforward as in the  $u - p_w$ , where it is a degree of freedom. In the proposed methodology, since it is calculated in the material points with the Eq. (6), and the strain state of the soil is defined by the material model, the deformation mapping of the water has to be defined for the initial step, even if there is no initial pore pressure since an equilibrium of Eq. (6) has to be reached.  $\mathbf{F}_w$  can be calculated as  $\exp[\text{tr}(\boldsymbol{\varepsilon}_w)/3]$ , where:

$$\text{tr}(\boldsymbol{\varepsilon}_w) = \text{div}(\mathbf{w}) = -\frac{p_{w0}}{Q} - \text{div}(\mathbf{u}) \quad (\text{Appendix A.3})$$

## Appendix B. Consistent Linearization

Following, the two main equations of the  $u - w$  formulation are presented since these are the equations that are implemented in order to be solved:

- Linear momentum of for the solid phase

$$\begin{aligned}
& - \int_B \text{grad}(\delta \mathbf{u}) : \mathbf{c}^{ep} : \text{grad}(\Delta \mathbf{u}) \, dv \\
& - \int_B \boldsymbol{\sigma}' : \text{grad}^T(\delta \mathbf{u}) \text{grad}(\Delta \mathbf{u}) \, dv \\
& - \int_B \text{grad}(\delta \mathbf{u}) : (Q [\text{div}(\Delta \mathbf{u}) + \text{div}(\Delta \mathbf{w})] \mathbf{I}) \, dv \\
& - \int_B \text{grad}(\delta \mathbf{u}) : p_w \text{grad}^T(\Delta \mathbf{u}) \, dv \\
& - \int_B \text{grad}(\delta \mathbf{u}) : p_w \frac{1-n}{n} \text{div}(\Delta \mathbf{u}) \mathbf{I} \, dv \\
& - \alpha_1 \int_B \delta \mathbf{u} \cdot [\rho \Delta \mathbf{u} + \rho_w \Delta \mathbf{w} + \rho_w \text{div}(\Delta \mathbf{u}) (\mathbf{u} + \mathbf{w})] \, dv \\
& + \int_B \rho_w \delta \mathbf{u} \cdot \mathbf{g} \text{div}(\Delta \mathbf{u}) \, dv \quad (\text{Appendix B.1})
\end{aligned}$$

335

- Linear momentum for the fluid phase:

$$\begin{aligned}
& - \int_B \text{grad}(\delta \mathbf{w}) : (Q [\text{div}(\Delta \mathbf{u}) + \text{div}(\Delta \mathbf{w})] \mathbf{I}) \, dv \\
& - \int_B \text{grad}(\delta \mathbf{w}) : p_w \text{grad}^T(\Delta \mathbf{u}) \, dv \\
& - \int_B \text{grad}(\delta \mathbf{w}) : p_w \frac{1-n}{n} \text{div}(\Delta \mathbf{u}) \mathbf{I} \, dv \\
& - \alpha_4 \int_B \frac{\mu_w}{k} \delta \mathbf{w} \cdot \left[ \Delta \mathbf{w} + \text{div}(\Delta \mathbf{u}) \left( 1 - \frac{1-n}{k} \frac{\partial k}{\partial n} \right) \mathbf{w} \right] \, dv \\
& - \alpha_1 \int_B \frac{\rho_w}{n} \delta \mathbf{w} \cdot \left[ \Delta \mathbf{w} + \frac{2n-1}{n} \text{div}(\Delta \mathbf{u}) \mathbf{w} \right] \, dv \\
& - \alpha_1 \int_B \rho_w \delta \mathbf{w} \cdot [\Delta \mathbf{u} + \text{div}(\Delta \mathbf{u}) \mathbf{u}] \, dv \\
& + \int_B \rho_w \delta \mathbf{w} \cdot \mathbf{g} \text{div}(\Delta \mathbf{u}) \, dv \quad (\text{Appendix B.2})
\end{aligned}$$

## References

- [1] M. T. Pastor, O. C. Zienkiewicz, A. H. C. Chan, Generalized plasticity and the modelling of soil behaviour, Int. J. Numer. Anal. Methods Geomech. 14 (1990) 151–190. doi:10.1016/j.ocecoaman.2012.02.008.

340

- [2] P. Mira, L. Tonni, M. T. Pastor, J. A. Fern, A generalized midpoint algorithm for the integration of a generalized plasticity model for sands 77 (2009) 1201–1223. doi:10.1002/nme.
- 345 [3] D. G. Manzanal, J. A. Fernández Merodo, M. T. Pastor, Generalized plasticity state parameter-based model for saturated and unsaturated soils. Part 1: Saturated state, Int. J. Numer. Anal. Methods Geomech. 35 (2011) 1347–1362. arXiv:nag.2347, doi:10.1002/nag.
- 350 [4] D. G. Manzanal, M. T. Pastor, J. A. Fernández Merodo, Generalized plasticity state parameter-based model for saturated and unsaturated soils. Part II: Unsaturated soil modeling, Int. J. Numer. Anal. Methods Geomech. 35 (2011) 1899–1917. arXiv:nag.2347, doi:10.1002/nag.
- 355 [5] O. C. Zienkiewicz, C. T. Chang, P. Bettles, Drained, undrained, consolidating and dynamic behaviour assumptions in soils, Géotechnique 30 (4) (1980) 385–395. doi:10.1016/j.ocecoaman.2012.02.008.
- [6] P. Navas, R. C. Yu, S. López-Querol, B. Li, Dynamic consolidation problems in saturated soils solved through u-w formulation in a {LME} meshfree framework, Comput. Geotech. 79 (2016) 55–72. doi:10.1016/j.compgeo.2016.05.021.
- 360 [7] S. López-Querol, Modelización geomecánica de los procesos de densificación, licuefacción y movilidad cíclica de suelos granulares sometidos a solicitaciones dinámicas, Ph.D. thesis, University of Castilla-La Mancha, Ciudad Real, Spain (2006).
- 365 [8] R. W. Lewis, B. A. Schrefler, The finite element method in the static and dynamic deformation and consolidation of porous media., John Wiley & Sons Ltd., 1998.
- [9] S. López-Querol, J. A. Fernández Merodo, P. Mira, M. T. Pastor, Numerical modelling of dynamic consolidation on granular soils, Int. J. Numer. Anal. Methods Geomech. 32 (2008) 1431–1457. arXiv:nag.2347, doi:10.1002/nag.
- 370 [10] O. C. Zienkiewicz, A. H. C. Chan, M. T. Pastor, B. A. Schrefler, T. Shiomi, Computational Geomechanics, John Wiley, UK, 1999.
- [11] K. V. Terzaghi, Principles of Soil Mechanics, Eng. News-Record 95 (1925) 19–27.



- 375 [12] S. Kontoe, Developement of time integration schemes and advanced  
boundary conditions for dynamic geotechnical analysis, Ph.D. thesis  
(2006).  
URL [http://ethos.bl.uk/OrderDetails.do?uin=uk.bl.ethos.  
435799](http://ethos.bl.uk/OrderDetails.do?uin=uk.bl.ethos.435799)
- 380 [13] P. Wriggers, Nonlinear Finite Element Methods, Springer, 2008.
- [14] P. Navas, L. Sanavia, S. López-Querol, R. C. Yu, u-w formu-  
lation for dynamic problems in large deformation regime solved  
through an implicit meshfree scheme., Comput. Mech. Published (4)  
(2017) <https://doi.org/10.1007/s00466-017-1524-y>. doi:10.1007/  
385 s00466-017-1524-y.  
URL <https://doi.org/10.1007/s00466-017-1524-y>
- [15] M. Arroyo, M. Ortiz, Local maximum-entropy approximation schemes:  
a seamless bridge between finite elements and meshfree methods, Int.  
J. Numer. Methods Eng. 65 (13) (2006) 2167–2202. doi:10.1002/nme.  
390 1534.
- [16] P. Navas, S. López-Querol, R. C. Yu, M. T. Pastor, Optimal trans-  
portation meshfree method in geotechnical engineering problems under  
large deformation regime, Int. J. Numer. Methods Eng. 115 (10) (2018)  
1217–1240. doi:10.1002/nme.5841.
- 395 [17] A. Cuitiño, M. Ortiz, A material-independent method for extending  
stress update algorithms from small-strain plasticity to finite plasticity  
with multiplicative kinematics, Eng. Comput. 9 (1992) 437–451.
- [18] G. T. Houlsby, A. Amorosi, E. Rojas, Elastic moduli of soils dependent  
on pressure: a hyperelastic formulation, Géotechnique 55 (5) (2005)  
400 383–392. doi:10.1680/geot.55.5.383.66021.
- [19] R. Santagiuliana, B. A. Schrefler, Enhancing the Bolzon-Schrefler-  
Zienkiewicz constitutive model for partially saturated soil, Transp.  
Porous Media 65 (1) (2006) 1–30. doi:10.1007/s11242-005-6083-6.
- 405 [20] F. BAHDA, Etude du comportaement du sable à l’appareil triaxial  
: expérience et modélisation, Ph.D. thesis, thèse de doctorat dirigée  
par CANOU, JEAN Sciences appliquées Marne-la-vallée, ENPC 1997  
(1997).  
URL <http://www.theses.fr/1997ENPC9730>